An improved k- model applied to a wind turbine wake in atmospheric turbulence

van der Laan, Paul; Sørensen, Niels N.; Réthoré, Pierre-Elouan; Mann, Jakob; Kelly, Mark C.; Troldborg, Niels; Schepers, J. Gerard; Machefaux, Ewan

Published in:
Wind Energy

Link to article, DOI:
10.1002/we.1736

Publication date:
2015

Document Version
Early version, also known as pre-print

WIND ENERGY
Wind Energ. 2013; **00**:1–19
DOI: 10.1002/we

RESEARCH ARTICLE

An improved k-ε model applied to a wind turbine wake in atmospheric turbulence

M. Paul van der Laan[1], Niels N. Sørensen[1], Pierre-Elouan Réthoré[1], Jakob Mann[1], Mark C. Kelly[1], Niels Troldborg[1], J. Gerard Schepers[2] and Ewan Machefaux[1]

[1]Department of Wind Energy, Technical University of Denmark, Risø campus, DK-4000 Roskilde, Denmark.
[2]Energy Research Centre of the Netherlands (ECN), Wind Energy, Petten, 1755ZG, The Netherlands.

ABSTRACT

An improved k-ε turbulence model is developed and applied to a single wind turbine wake in a neutral atmospheric boundary layer using a Reynolds averaged Navier-Stokes solver. The proposed model includes a flow-dependent C_μ that is sensitive to high velocity gradients, e.g. at the edge of a wind turbine wake. The modified k-ε model is compared with the original k-ε eddy viscosity model, Large-Eddy Simulations and field measurements using eight test cases. The comparison shows that the velocity wake deficits, predicted by the proposed model are much closer to the ones calculated by the Large-Eddy Simulation and those observed in the measurements, than predicted by the original k-ε model. Copyright © 2013 John Wiley & Sons, Ltd.

KEYWORDS

k-ε eddy viscosity model; wind turbine wakes; actuator disc; CFD; RANS; LES.

Correspondence

M. Paul van der Laan, Department of Wind Energy, Technical University of Denmark, Risø campus, DK-4000 Roskilde, Denmark.
Email: plaa@dtu.dk.

Received . . .

1. INTRODUCTION

The energy losses in a wind farm due to the effects of wind turbine wakes can often range between 10% to 20% [1]. Wind turbine wakes also increase turbulence levels and can lead to early fatigue of wind turbines downstream. Therefore reliable and practical modeling of the influence of wind turbine wakes in wind farms is necessary, in order to estimate the wind farm annual energy production and the wind turbine loads. Wake effects have been studied using many tools, ranging from simple empirical engineering models to Computational Fluid Dynamics (CFD) methods such as Reynolds average Navier-Stokes (RANS) or Large-Eddy Simulation (LES). LES results have proven to compare well with results of wake measurements [2], but the computational costs are still high, especially if complete wind farms are considered. RANS is roughly three orders of magnitude less of computational resources than LES (as illustrated in Sec. 4.2.3), however, previous studies have shown that the most widely used turbulence models in RANS, e.g. the (linear) k-ε eddy viscosity model (EVM), fail to predict the wake deficit and the Reynolds-stresses in a wake [3, 4, 5, 6]. The basis of a linear EVM is the eddy viscosity hypothesis of Boussinesq, which linearly relates the Reynolds-stresses to the symmetrical part of the velocity gradients [7]. Boussinesq hypothesis is seldom valid and can only predict isotropic turbulence [8]. Therefore, the k-ε EVM cannot describe the anisotropic turbulence that is present in a neutral atmospheric boundary layer (ABL) nor in a wind turbine wake. In addition, the parameter C_μ present in definition of the eddy viscosity is a constant in the k-ε EVM, which makes the model too dissipative when it is employed for a wake.

Modifications of the k-ε EVM have been proposed and tested successfully for wind turbines wakes. El Kasmi and Masson [5] used an extra source term in the dissipation equation of the k-ε EVM (originally proposed by Chen and Kim [9]), which is only active in the vicinity of rotor. This source term includes a constant $C_{\varepsilon,4}$ that, together with the size of region where the source term is applied, determines the performance of the model. El Kasmi and Masson showed that the source term improves the velocity deficit for several cases compared to single wake measurements. Unfortunately, a

thorough calibration of the source term is not published in the work of El Kasmi and Masson. Prospathopoulos et al. [6] and Réthoré [3] investigated the modified k-ε EVM of El Kasmi and Masson, using different values of $C_{\varepsilon,4}$, while keeping the region of activity constant. Their work shows that the value of $C_{\varepsilon,4}$ is not general and needs to be adjusted for different single wind turbine wake cases. In addition, Prospathopoulos et al. showed that if the source term is calibrated to describe the velocity wake deficit at the far wake, it may not perform well in the near wake and vice versa. It should be noted that Prospathopoulos et al. and El Kasmi and Masson only compared the modified k-ε EVM with measurements, not with LES, which can lead to an unfair comparison due to uncertainties in measurements. Cabezón et al. [4] investigated another modified k-ε EVM, known as the realizable k-ε EVM of Shih [10]. The model has a variable C_μ that is complex scalar function of the local flow, i.e. a flow-dependent C_μ, and it has a new transport equation for the dissipation rate. Cabezón et al. showed that the velocity deficit and the Reynolds-stresses (in some extend) predicted by the realizable k-ε EVM compares better with those of LES and measurements, with respect to the standard k-ε EVM. However, Cabezón et al. only considered one test case.

Another type of alternative eddy viscosity models are the nonlinear eddy viscosity models (NLEVMs). Instead of using the traditional Boussinesq hypothesis, the NLEVMs are based on a nonlinear stress-strain relationship in which products of the velocity gradients are present. In addition, the NLEVMs often have a flow-dependent C_μ that has similar behavior as the flow-dependent C_μ of the realizable k-ε EVM of Shih [10]. In previous work, modified versions of the cubic NLEVM of Apsley and Leschziner [11] and the quartic NLEVM of Taulbee [12] have been employed for wind turbine wake simulations [13]. The NLEVM of Taulbee is also applied to a single wind turbine wake in the work of Gomez-Elvira et al. [14]. In terms of wake deficit and Reynolds-stresses, the performance of these NLEVMs is improved compared to the k-ε EVM. The nonlinear terms in the stress-strain relationship can model anisotropic turbulence and this is the main reason for the improved Reynolds-stress predictions. The flow-dependent C_μ lowers the eddy-viscosity downstream of the wind turbine, which increases the wake deficit. As a result, the wake deficit predicted by the NLEVMs is closer to the one calculated by LES and observed in measurements. Unfortunately, the tested NLEVMs show numerically unstable behavior for high turbulence levels [13]. In addition, it has been found that the cubic and the quartic NLEVMs are not stable for fine grids, which is a major problem for grid refinement studies.

The goal of the present research is to develop a general RANS-based turbulence model that solves the shortcomings of the k-ε EVM, without losing its simplicity and numerical stability. In addition, a model is desired that is general for a large range of different wind turbine wake cases and does not need recalibration. In this paper, a modified k-ε EVM is presented that has a flow-dependent C_μ, which we label as the k-ε-f_P EVM. f_P is a scalar function that includes variability of the flow-dependent C_μ. Hereafter, the flow-dependent C_μ is referred as C_μ^*, i.e, $C_\mu^* = C_\mu f_P$ with C_μ as the traditional constant from the standard k-ε EVM. The proposed model is a simplified version of the cubic NLEVM of Apsley and Leschziner [11], in which the nonlinear terms in the stress-strain relationship are disregarded. By removing the nonlinear terms, the model is stable for the practical range of turbulence levels and grid spacings. Hence a grid refinement study is feasible, and the results show that the model becomes grid-independent for fine enough grids, as discussed in Sec. 4.1.1. Since the proposed model is linear, only isotropic turbulence can be predicted, and one should not expect to observe significant improved Reynolds-stresses compared to the original k-ε EVM, as observed for NLEVMs in the work of van der Laan et al. [13]. Therefore, the current work focuses on improving the wake deficit. An advantage of the k-ε-f_P EVM over the modified k-ε EVM of El Kasmi and Masson [5], is that the k-ε-f_P EVM lets the flow decide where the modification is active, instead of using an arbitrary region in which it should be activated.

The k-ε-f_P EVM is presented in Sec. 2, where the effect of C_μ^* is discussed. Sec. 2, also shows that the relation of C_μ^* in the k-ε-f_P EVM is very similar to the one of the realizable k-ε EVM of Shih [10], however, it is much simpler and has only one constant to calibrate, namely the Rotta constant C_R. The constant C_R can be used to fit a certain measurement, however, it would be preferable not to calibrate the turbulence model each time a flow parameter is changed. Therefore, a comprehensive calibration of C_R in the k-ε-f_P EVM is presented in Sec 4, in which eight single-wake cases are used. Four of the eight single-wake cases are based on field measurements and they are discussed in Sec. 3. Section 4 also covers the simulation methods, and a comparison is made between the k-ε-f_P EVM, original k-ε EVM, LES and available measurements.

2. MODEL DESCRIPTION

In Sec. 2.1 a brief description of the proposed k-ε-f_P EVM is presented. The background and the effect of C_μ^* is discussed in Sec. 2.2. Note that repetitive indices are summed and an index after a comma represents a derivative.

2.1. Definition

The stress-strain relationship in the k-ε-f_P EVM is exactly the same as the standard k-ε EVM:

$$\overline{u_i' u_j'} = \frac{2}{3} k \delta_{ij} - \nu_T \left(U_{i,j} + U_{j,i} \right), \tag{1}$$

Wind Energ. 2013; **00**:1–19 © 2013 John Wiley & Sons, Ltd.
DOI: 10.1002/we
Prepared using weauth.cls

with $\overline{u_i' u_j'}$ as the Reynolds-stress, k as the turbulent kinetic energy, δ_{ij} as the Kronecker delta and $U_{i,j}$ as the mean velocity gradient. The turbulent eddy viscosity ν_T in the proposed model is different from the standard k-ε EVM but has the same form:

$$\nu_T = C_\mu^* \frac{k^2}{\varepsilon}, \tag{2}$$

with ε as the turbulent dissipation and C_μ^* as a flow-dependent parameter which is a constant in the original k-ε EVM, i.e. C_μ. The flow-dependent parameter C_μ^* is defined as [11]:

$$C_\mu^* = C_\mu f_P, \tag{3}$$

in which f_P is a scalar function that models the effect of non-equilibrium flow conditions [11]:

$$f_P\left(\sigma/\tilde{\sigma}\right) = \frac{2f_0}{1+\sqrt{1+4f_0\left(f_0-1\right)\left(\frac{\sigma}{\tilde{\sigma}}\right)^2}},\ f_0 = \frac{C_R}{C_R-1}, \tag{4}$$

with C_R as the Rotta constant, originally chosen as 1.8 [15]. Eq. 4 is motivated in Sec. 2.2. The shear parameter $\sigma \equiv \frac{k}{\varepsilon}\sqrt{\left(U_{i,j}\right)^2}$ is used to quantify how far the local flow deviates from the log law regime of a simple shear flow, for which the k-ε-f_P EVM is calibrated. In the calibration flow the shear parameter σ is equal to $\tilde{\sigma}$, i.e. $\tilde{\sigma} = \frac{k}{\varepsilon}\left\|\frac{\partial U}{\partial z}\right\| = 1/\sqrt{C_\mu}$, using the log law solution of the k-ε EVM [16]. Hence, f_P is also a function of C_μ, i.e., $f_P\left(C_\mu\right)$.

The k-ε-f_P model uses the same transport equations for k and ε as employed in the original k-ε EVM:

$$\frac{Dk}{Dt} = \nabla\cdot\left[\left(\nu+\frac{\nu_T}{\sigma_k}\right)\nabla k\right] + \mathcal{P} - \varepsilon, \qquad \frac{D\varepsilon}{Dt} = \nabla\cdot\left[\left(\nu+\frac{\nu_T}{\sigma_\epsilon}\right)\nabla\varepsilon\right] + \left(C_{\varepsilon,1}\mathcal{P} - C_{\varepsilon,2}\varepsilon\right)\frac{\varepsilon}{k}, \tag{5}$$

where ν is the kinematic molecular viscosity, $\mathcal{P}$ is the turbulent production and $C_{\varepsilon,1}, C_{\varepsilon,2}, \sigma_k, \sigma_\varepsilon$ are constants. In total, seven model constants exist in the k-ε-f_P EVM, which are summarized in Table I. The traditional k-ε EVM constants are chosen to be able to describe a neutral atmospheric boundary layer in which $C_\mu = 0.03$ and $C_{\varepsilon,1}$ is set such that the log law solution is recovered. The constant C_R is calibrated with LES, as discussed in Sec. 4.

Table I. Model constants.

C_R	C_μ	$C_{\varepsilon,1}$	$C_{\varepsilon,2}$	σ_k	σ_ε	κ
4.5	0.03	1.21	1.92	1.00	1.30	0.40

2.2. The f_P function

Apsley and Leschziner [11] introduced the limiter function f_P (Eq. 4) to bound the nonlinear terms of their cubic NLEVM and extend it to non-equilibrium conditions. In the cubic NLEVM, f_P is also used to obtain the relation for C_μ^*, similar to Eq. 3. In the present research, the relation for C_μ^* is adopted, but all nonlinear terms are disregarded. Hence, the standard linear k-ε EVM is recovered, including a variable C_μ. Apsley and Leschziner derived their cubic NLEVM from an algebraic Reynolds-stress model in an approximate manner, with algebraic Reynolds-stress parameters α, β and γ that are proportional to $1/(C_R + \mathcal{P}/\varepsilon - 1)$. C_R represents the constant in the "slow" part of the pressure-strain model of Launder et al. [17, 18]. $\mathcal{P}/\varepsilon$ is the ratio of turbulent production to dissipation. The derived cubic NLEVM includes the same parameters α, β and γ; however, they are used to calibrate the cubic NLEVM with a simple shear flow. Therefore, one can suggest to multiply the calibrated α, β and γ in the cubic NLEVM with a factor:

$$f_P = \frac{C_R + \widetilde{\mathcal{P}/\varepsilon} - 1}{C_R + \mathcal{P}/\varepsilon - 1}, \tag{6}$$

in which $\widetilde{\mathcal{P}/\varepsilon}$ is the ratio of turbulent production and dissipation in the calibration flow, i.e., $\widetilde{\mathcal{P}/\varepsilon} = 1$. Apsley and Leschziner found that the direct use of Eq. 6 is numerically unstable, and proposed the approximation $\mathcal{P}/\varepsilon \approx f_P C_\mu \sigma^2$, which is adopted in the present research. This approximation, and using $\widetilde{\mathcal{P}/\varepsilon} = C_\mu\tilde{\sigma}^2$, leads to Eq. 4.

The behavior of C_μ^* is plotted in Fig. 1 in terms of f_P for the original and the calibrated value of C_R; 1.8 and 4.5, respectively. For comparison a normalized C_μ^* of Shih [10] is also shown, which is discussed in the next paragraph. f_P is unity when the flow is in equilibrium ($\sigma = \tilde{\sigma}$, irrespective of f_0) and C_μ^* is equal to C_μ. For $\sigma > \tilde{\sigma}$, $f_P < 1$, C_μ^* is lower

than C_μ. As a result, the eddy viscosity from Eq. 2 is lowered and the k-ε-f_P EVM behaves less dissipatively for high shear parameters compared to the original k-ε EVM. In the near-wake of a wind turbine σ can be much larger than $\tilde{\sigma}$, hence, C_μ^* has a high impact on the flow solution, which is mainly seen in the wake deficit, as shown in Sec. 4. When C_R is increased the effect of f_P is reduced, and the model behavior of the k-ε-f_P EVM will approach that of the original k-ε EVM. In terms of wake deficit, increasing C_R will enhance the wake recovery, hence, C_R controls the flow solution and should be carefully chosen. Instead of using the original value of 1.8, a comprehensive calibration of C_R is carried out in Sec. 4.

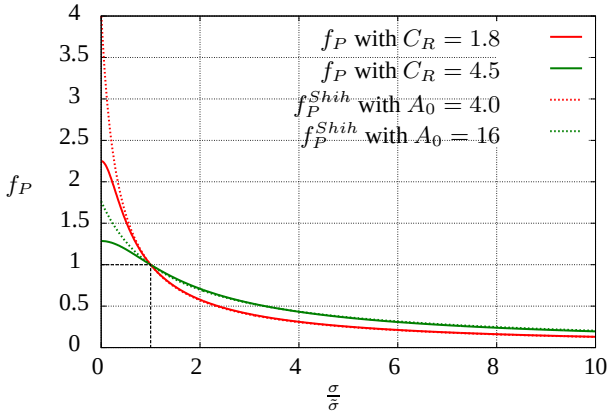

Figure 1. f_P of k-ε-f_P EVM and f_P^{Shih}, derived from the realizable k-ε EVM of Shih, in a stationary frame of reference with $S_{kl}S_{lm}S_{mk} = 0$.

Another C_μ^* function is developed by Shih [10], which is derived using realizability arguments. This C_μ^* function is part of the realizable k-ε EVM of Shih, which Cabezón et al. [4] tested successfully for wind turbine wake simulations. The function can be written in the form of Eq. 4 (in a stationary frame of reference):

$$f_P^{Shih} \equiv \frac{C_\mu^*}{C_\mu^*\,|_{\sigma=\tilde{\sigma}}} = \frac{f_0}{1+(f_0-1)\,\frac{\sigma}{\tilde{\sigma}}}, \qquad f_0 = 1+\tilde{\sigma}\frac{A_s}{A_0},$$
$$A_s = \sqrt{6}\cos\left[1/3\arccos\left(\sqrt{6}\frac{S_{kl}S_{lm}S_{mk}}{(S_{kl}S_{lk})^{(3/2)}}\right)\right], \tag{7}$$

where A_0 is a constant, originally set to 4.0 [10]. A_s is a complex relation of traces of products of the strain-rate tensor $S_{ij} \equiv 1/2\,(U_{i,j}+U_{j,i})$. Note that the normalization is done with $C_\mu^*\,|_{\sigma=\tilde{\sigma}}$, such that a comparison can be made with the limiter function f_P of Apsley and Leschziner. For $S_{kl}S_{lm}S_{mk} = 0$ (valid in the log law region of the ABL and for 2D flows), $A_s = 3/2\sqrt{2}$ and f_P^{Shih} is very similar to the f_P with $C_R = 1.8$, especially for $\frac{\sigma}{\tilde{\sigma}} > 1$. Deviations between f_P^{Shih} and f_P are observed for $\frac{\sigma}{\tilde{\sigma}} < 1$. In addition, Fig. 1 shows that increasing A_0 ($A_0 = 16$) has a similar effect as increasing C_R. In principle f_P^{Shih} can also be applied in the k-ε-f_P EVM instead of f_P, however, it has been found that f_P is more robust compared to f_P^{Shih}.

3. TEST CASES

The k-ε-f_P EVM is used to simulate the wake of a single wind turbine for eight test cases. An overview of the test cases is given in Tab. II. The first two test cases are based on meteorological mast wake measurements from the Wind Turbine Test Site Wieringermeer (EWTW), owned by the Energy Research Centre of the Netherlands (ECN) [19]. The third test case is based on an old measurement campaign, namely the field wake measurements of the Nibe B wind turbine conducted in Denmark [20]. The fourth test case is derived from a set of recent lidar measurements of a Nordtank 500 test wind turbine, owned and maintained by the Technical University of Denmark (DTU) [21, 22]. Finally four additional test cases are defined to investigate the influence of the undisturbed turbulence intensity at hub height $I_{H,\infty} \equiv \sqrt{(2/3k)}/U_H$ and the thrust coefficient C_T. These parameters are considered as the most important ones for a wind turbine wake in a neutral atmospheric boundary layer, since other parameters are either used to normalize the wake deficit (undisturbed wind speed at hub height $U_{H,\infty}$ and rotor diameter D) or else they can be related to the turbulence intensity (roughness height z_0, friction velocity u_* and hub height z_H). In addition, the rotational force component is not expected to play a large role in

Wind Energ. 2013; **00**:1–19 © 2013 John Wiley & Sons, Ltd.
DOI: 10.1002/we
Prepared using weauth.cls

the wake deficit compared to the thrust coefficient. The four additional test cases are based on the NREL 5 MW reference wind turbine [23]. The high undisturbed turbulence intensity in case 6 is chosen to reflect the maximum stream-wise undisturbed turbulence intensity of 16%, using Eq. 9. In the last two test cases only C_T is changed while other parameters (C_P, $U_{H,\infty}$, etc.) are kept the same. This approach leads to a setup that does not resemble the C_P and C_T dependency on wind speed that correspond to the original NREL-5MW wind turbine, however, the influence of C_T on the wake deficit can now be investigated.

In order to compare the measurements with the numerical simulations the following input parameters for the numerical simulations are necessary: the undisturbed turbulence intensity at hub height $I_{H,\infty}$, the thrust coefficient C_T, the power coefficient C_P, the rotational speed Ω, the undisturbed wind speed at hub height $U_{H,\infty}$, the rotor diameter D and the hub height z_H. The roughness height z_0 and the undisturbed friction velocity u_* are not input parameters for the simulations, because these parameters will be used to control the turbulence intensity at hub height as discussed in Sec. 4.1.1. The test cases that are based on measurements are described in the following sections.

Table II. Summary of cases and corresponding input parameters for numerical computations.

Case	Description	Measurement data	$I_{H,\infty}$ [-]	C_T [-]	C_P [-]	Ω [RPM]	$U_{H,\infty}$ [m/s]	D [m]	z_H [m]
1	Wieringermeer West	Met. mast, 4.5 years, 3.5D	8.0%	0.63	0.44	19.1	10.7	80	80
2	Wieringermeer East	Met. mast, 4.5 years, 2.5D	6.0%	0.63	0.44	19.1	10.9	80	80
3	Nibe B	Met. mast, 2 years, 2.5D,4D,7.5D	8.0%	0.89	0.46	34	8.5	40	45
4	Nordtank 500	Lidar, 102x10 minutes, 1D,2D,3D,4D,5D	11.2%	0.70	0.44	27.1	7.45	41	36
5	NREL-5MW Low $I_{H,\infty}$	-	4.0%	0.79	0.47	9	8.0	126	90
6	NREL-5MW High $I_{H,\infty}$	-	12.8%	0.79	0.47	9	8.0	126	90
7	NREL-5MW Low C_T	-	8.0%	0.50	0.47	9	8.0	126	90
8	NREL-5MW High C_T	-	8.0%	0.90	0.47	9	8.0	126	90

3.1. Wieringermeer

ECN Wind Turbine Test Site is located in Wieringermeer, an area in the North West of the Netherlands. The landscape mainly consist of flat farmland. 2 km East from the meteorological mast a large lake (IJsselmeer) is present. The land and the lake are separated by a dike which rises 8 m and 3 m above the land and the lake, respectively. The meteorological mast is located South of five 2.5 MW Nordex wind turbines, all with a 80 m rotor diameter and hub height. The layout of the five wind turbine positions is given in Fig. 2. Two single wake cases are measured for wind directions around 31°and 315°with a corresponding downstream distance of 2.5D and 3.5D, respectively. The results of almost five years of measurements have been published by Schepers et al. [19]. In addition, the ten minute averaged data was made available for this research.

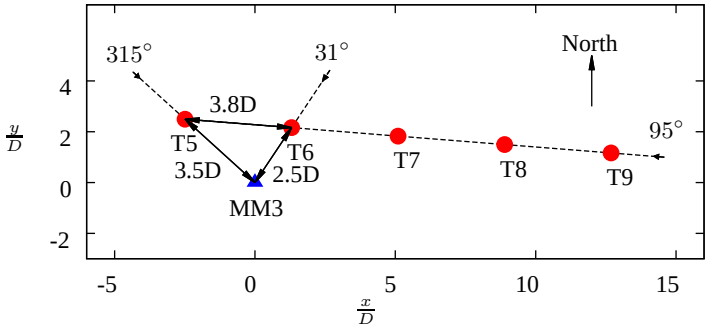

Figure 2. Sketch of wind turbines (red dots) and meteorological mast (blue triangle) at EWTW site.

The meteorological mast is instrumented with sonic anemometers, cups and vanes at 80 m. Unfortunately, upstream measurements are not carried out. Therefore, the upstream undisturbed wind speed at hub height is estimated from power measurements of wind turbine T5 (Eastern wake case) and wind turbine T6 (Western wake case). Only data with undisturbed wind speeds between 10-12 m/s is selected, which is the highest wind speed bin available. The average wind speed between 1-61°and 285-345°, corresponding to the two single wake cases, are 10.9 m/s and 10.7 m/s, respectively. The lack of upstream measurements makes it impossible to identify and disregard non-neutral atmospheric measurements. However, the probability of a near neutral ABL increases with high wind speeds, i.e. 10-12 m/s. Another important

consequence of missing upstream measurements, is the fact that the undisturbed turbulence intensity cannot be directly measured for the wind direction of single wake cases. Schepers et al. [19] estimated the undisturbed stream-wise turbulence intensities $I_{u,H,\infty} \equiv \sigma_u/U_H$ (outside the region of wind directions corresponding to the single wake cases) to be 10% and 7.5% for the Western and Eastern wind directions, respectively. Since the three standard deviations of the velocity components σ_u, σ_v and σ_w are not all available, the total turbulence intensity $I_{H,\infty}$ is estimated from the standard ratios:

$$\frac{\sigma_v}{\sigma_u} = 0.8, \qquad \frac{\sigma_w}{\sigma_u} = 0.5, \tag{8}$$

which have been measured by Panofsky and Dutton [24] and are adopted in the IEC 61400-1 standard [25]. This leads to:

$$I_{H,\infty} = I_{u,H,\infty}\sqrt{\frac{1}{3}\left(1 + 0.8^2 + 0.5^2\right)} \approx 0.8 I_{u,H,\infty}, \tag{9}$$

hence, the total turbulence intensity $I_{H,\infty}$ is estimated to be 8% and 6% for the Western and Eastern wind directions, respectively.

The thrust coefficient curve is measured and calculated by Schepers [26]. The measurements are based on the tower bending moment and the calculations are carried out with PHATAS [27]. Both methods estimate a thrust coefficient of 0.63 for the averaged undisturbed wind speeds of 10.7 m/s and 10.9 m/s.

The mechanical power curve is not available. Therefore, it is estimated from the electrical power curve (given by the wind turbine manufacturer Nordex) assuming a loss of 6%. This gives a power coefficient of 0.44 for both Wieringermeer cases.

The Nordex wind turbine has variable rotational speeds ranging from 10.9 RPM to 19.1 RPM. The dependency of the rotational speed on the wind speed is not available. For the present research it is assumed that the rotor is rotating with 19.1 RPM.

3.2. Nibe

In the 1980s field measurements of two wind turbines at Nibe, in Northern Denmark, were conducted by Taylor [20]. The wind turbines have a hub height and rotor diameter of 45 m and 40 m, respectively. The two wind turbines are located at five rotor diameters away from each other. The Nibe B wind turbine is located South from Nibe A wind turbine. A sketch of the layout is shown in Fig. 3. Four meteorological masts are placed in a line at downstream distances: 2.5D, 4D, 6D and 7.5D with respect to the Nibe B wind turbine. The masts are instrumented with cup anemometers at several heights. The selected data set includes wind directions from the South, which corresponds to inflow condition over land with a relatively flat terrain. For the current single wake case of the Nibe B wind turbine, the Nibe A wind turbine is not operational, however, an influence of the Nibe A wind turbine on the downstream meteorological masts at 6D and 7.5D cannot be avoided. For this reason, the data at 6D (MM3, located at 1D from the Nibe A wind turbine) is disregarded.

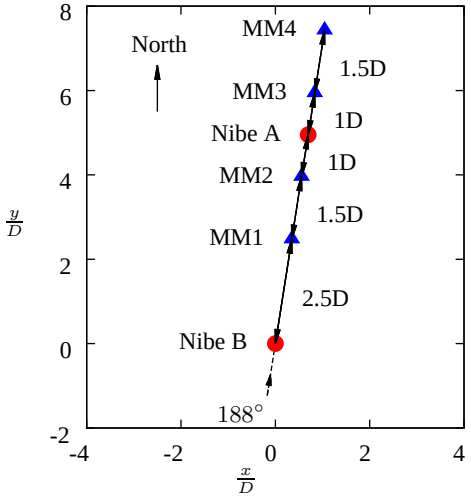

Figure 3. Sketch of wind turbines (red dots) and meteorological masts (blue triangles) at Nibe.

The chosen data set consist of 1 min. averages, taken over a period of about 2 years. The averaged velocity of 8.5 m/s is obtained from power measurements and the known power curve.

Wind Energ. 2013; **00**:1–19 © 2013 John Wiley & Sons, Ltd.
DOI: 10.1002/we
Prepared using weauth.cls

Due to lack of upstream measurements, the undisturbed stream-wise turbulence intensity is estimated from a cup anemometer located at the mast at 2.5D downstream from Nibe B, at a height of 3 m. It is assumed that the wake of the Nibe B turbine has not expanded far enough to influence the measurement at this location [20]. Unfortunately, this estimate of the undisturbed stream-wise turbulence intensity is not very accurate because the influence of local surface variations can be significant at 3 m. The rough estimate gives an undisturbed stream-wise turbulence intensity of $I_{u,H,\infty} \approx 10\%$ which corresponds to a total turbulence intensity of $I_{H,\infty} \approx 8\%$ using Eq 9.

Filtering out non-neutral atmospheric measurements has not been been carried out.

The thrust coefficient C_T is estimated as an average of an LES actuator line simulation in which tabulated airfoil data is used to calculated the blade forces. More details about this simulation can be found in the work of Troldborg et al. [28]. The method gives a C_T of 0.89, which also corresponds to the calculated thrust curve given in the work of Taylor [20]. The power coefficient could also be taken from the same LES actuator line simulation; however, it has been found that the LES actuator line simulation overestimates the power. [29, 30]. Therefore, the power coefficient $C_P = 0.46$ is estimated from the measured mechanical power curve, given by Taylor [20]. In addition, the rotational speed is also noted by Taylor: $\Omega = 43$ RPM.

3.3. Nordtank 500

A test site consisting of three wind turbines is situated on the Risø campus of DTU. An overview is sketched in Fig. 4. From left to right, the order of wind turbines is as follows: Tellus wind turbine, 95 kW, $D = 18$ m, $z_H = 29$ m, Nordtank 500 wind turbine (NTK), 500 kW, $D = 41$ m, $z_H = 36$ m, Vestas V27 wind turbine (V27), 225 kW, $D = 27$ m, $z_H = 30$ m. In addition, there is a meteorological mast (MM) at 2.2D West from the Nordtank 500 wind turbine. During the measurement campaign the rotor of the Vestas V27 wind turbine was taken down. The prevailing wind direction is South East, therefore, only data is selected for wind directions between 120°to 150°. The single wake of the Nordtank 500 wind turbine is measured using a nacelle mounted pulsed lidar. Details of this measurement campaign can be found in the work of Machefaux et al. [21, 22]. The lidar is used to scan the wake in a cross section at five downstream locations between 1D and 5D with a uniform spacing of 1D. The meteorological mast is instrumented with cup and sonic anemometers at several heights. Only the results at a height of 52.5 m are used from this mast, in order to prevent the wake influence of the Tellus wind turbine.

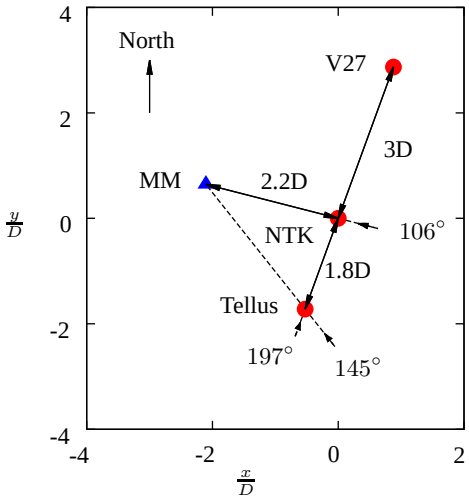

Figure 4. Sketch of wind turbines (red dots) and meteorological mast (blue triangle) at the Risø campus of the Technical University of Denmark. Distances are normalized with the rotor diameter of the Nordtank 500 (NTK) wind turbine: $D = 41$ m.

The undisturbed velocity at hub height is calculated from power measurements and the known power curve. This velocity is also directly measured at the meteorological mast at hub height, however, these measurements are influenced by the wake of Tellus wind turbine. In total 102 samples of approximately 10 min. averages are selected, with a velocity of 7-8 m/s and wind directions between 120°to 150°. This represents almost 17 hours of data, and its average velocity is calculated as 7.45 m/s.

The Obukhov length L is calculated from the sonics at the meteorological mast and it is used to identify the stability class of the measurements. It is found that the atmospheric conditions during the time of measurements are neutral: $(\text{mean}(\text{abs}(L)) = 7.5 \times 10^2)$ [22].

The thrust coefficient C_T is estimated from the tower bending moment which gives $C_T = 0.70$.

The meteorological mast is used to estimate the undisturbed turbulence intensity. Since the Tellus wind turbine wake influences the measurements at the meteorological mast around hub height, the turbulence intensity $I_{M,\infty}$, obtained from a sonic located at a height: $z_M = 52.5$ m is used. The undisturbed turbulence intensity at hub height is estimated by using the log law and assuming that $\sigma_u = Au_*$ is constant with height. Hence,

$$I_{H,\infty} = \frac{I_{M,\infty}}{1 - \frac{I_{u,M,\infty}}{\kappa A} \ln\left(\frac{z_M}{z_H}\right)}, \tag{10}$$

where κ is the Von Karman constant and A is function of the roughness height. Following Panofsky and Dutton [24], $A = 2.4$. Using Eq. 10 the measured total turbulence intensity at the mast ($I_{M,\infty} = 10.7\%$) is extrapolated to the hub height: $I_{H,\infty} = 11.2\%$ which is equivalent to a stream-wise turbulence intensity of 14% using Eq. 9.

4. SIMULATIONS

4.1. Method

The in-house incompressible finite volume code EllipSys3D is used as the flow solver, which can perform RANS and LES simulations [31, 32]. The Navier-Stokes equations are solved with the SIMPLE algorithm [33], and the QUICK scheme [34] is used to discretize the convective terms. The flow variables are stored in a co-located manner. To avoid decoupling of the pressure with body forces, the pressure equation is solved with a modified Rhie-Chow algorithm [35, 36].

The wind turbine is modeled as an Actuator Disk (AD) [37, 3, 38] on which the blade forces are distributed in the radial direction and constant in the circumferential direction. The blade force distributions that are applied on the AD are calculated with a full rotor detached eddy simulation (Nordtank 500 and NREL 5 MW) or are calculated with a LES simulation using an actuator line method including airfoil data (Nibe B) [28]. The result for the normal and the tangential force distributions are shown in Fig. 5. The radial blade force is not applied to the AD because it is often smaller than 1% of the normal blade force. The real blade geometry of the Nordex wind turbine from EWTW is not available. Therefore, the detached eddy simulation of the NREL 5 MW wind turbine blade is used, in which the original tangential ($q_T(r/R)$) and normal blade force distribution ($q_N(r/R)$) are scaled. First $q_T(r/R)$ and $q_N(r/R)$ are scaled to cover the desired rotor radius R. Subsequently, $q_T(r)$ and $q_N(r)$ are individually scaled with C_P, Ω and C_T, respectively. In addition, both distributions are scaled with $U_{H,\infty}$, R and ρ to obtain the tangential ($q_T^{AD}(r)$) and normal blade force distribution ($q_N^{AD}(r)$) that are applied to the AD:

$$\begin{aligned} q_N^{AD}(r) &= \hat{q}_N(r)\frac{1}{n}\frac{1}{2}\rho U_{H,\infty}^2 \pi R^2 C_T, & \hat{q}_N(r) &= \frac{q_N(r)}{\int_0^R q_N(r)dr}, \\ q_T^{AD}(r) &= \hat{q}_T(r)\frac{1}{n}\frac{\frac{1}{2}\rho U_{H,\infty}^3 \pi R^2 C_P}{2\pi\Omega/60}, & \hat{q}_T(r) &= \frac{q_T(r)}{\int_0^R q_T(r)rdr}, \end{aligned} \tag{11}$$

where $n = 3$ is the number of blades and $\hat{q}(r)$ denotes a normalized blade force distribution. The total normal force F_N and the power P are obtained by integration:

$$\begin{aligned} F_N &= n\int_0^R q_N^{AD}(r)dr = \frac{1}{2}\rho U_{H,\infty}^2 \pi R^2 C_T, \\ P &= 2\pi\Omega/60 n\int_0^R q_T^{AD}(r)rdr = \frac{1}{2}\rho U_{H,\infty}^3 \pi R^2 C_P. \end{aligned} \tag{12}$$

The scaling equations can easily be verified by taking analytical force distributions for the original blade, e.g.: $q_N(r) = -q_T(r) = -r(r-R)/R^2$, and substitute these relations into Eq. 11.

The input parameters from Table II are used in all AD simulations. Standard values for the density and the dynamic fluid viscosity are used: $\rho = 1.225$ kg/m^3 and $\mu = 1.784 \times 10^{-5}$ kg/(m·s) (corresponding to a temperature of 15 °C at sea level). It should be noted that the fluid viscosity is negligible compared to the eddy-viscosity, since the Reynolds number (based on the rotor diameter and the hub height velocity) is in the order of 10^7.

4.1.1. RANS

In the RANS simulations, the AD is placed in a box shaped domain of dimensions: 25D × 16D × 16D, as shown in Fig. 6. In total 1.18 million cells are used to discretize the domain. The boundary at $z = 0$ is modeled as a rough wall where the first cell height is on the order of the roughness height. In EllipSys3D, a rough wall is modeled by placing the flow domain on top of the roughness height. The wall stress and the turbulent dissipation are specified at the first cell,

DOI: 10.1002/we
Prepared using weauth.cls

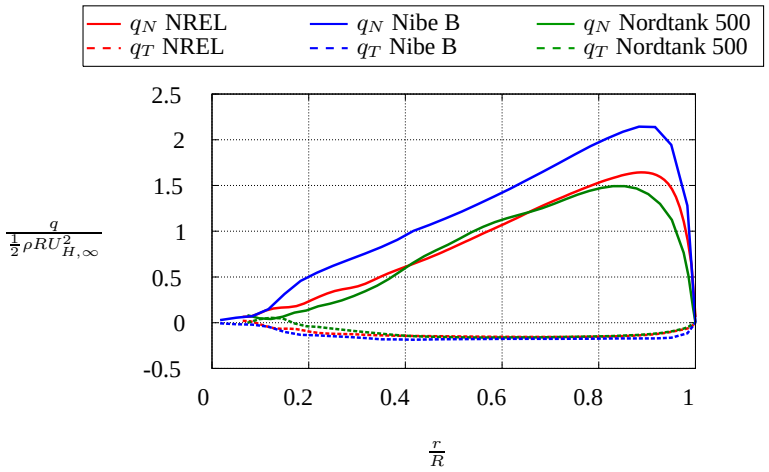

Figure 5. Calculated tangential q_T and normal force q_N distributions [n/m].

using the analytical expressions of the log law. In addition, a Neumann boundary condition is used for the turbulent kinetic energy. The top boundary at $z = 16$D and the boundaries at $x = 0$ are inlets, whereas, the boundary at $x = 25$D is an outlet. At the inlet a stream-wise logarithmic profile is specified:

$$U = \frac{u_*}{\kappa} \ln\left(\frac{z}{z_0}\right). \tag{13}$$

A Neumann boundary condition is applied on the outlet boundary. The side boundaries at $y = 0$ and $y = 16$D are modeled as slip walls. Around the AD a wake domain of dimensions: $14\text{D} \times 3\text{D} \times 3\text{D}$ is defined where uniform spacing of D/10 is applied in all directions. (Below $z = 1/2 z_H$ the cells in the wall normal direction are refined due to the presence of the wall.) The grid study in the section below shows that eight cells per diameter is sufficient. Outside the wake domain stretching is allowed with a maximum edge growth ratio of 1.2.

Setting the turbulence level in RANS via z_0

In the RANS modeling of atmospheric flows using the standard k-ε EVM, it is common to control the ambient turbulence intensity at hub height $I_{H,\infty}$:

$$I_{H,\infty} \equiv \frac{\sqrt{\frac{2}{3}k}}{U_{H,\infty}} = \frac{\kappa\sqrt{\frac{2}{3}}}{\ln\left(\frac{z_H}{z_0}\right)\sqrt[4]{C_\mu}}, \tag{14}$$

by changing C_μ and adapting one of the other model constants such that the log law solution (Eqs. 13) is maintained: $\sqrt{C_\mu}\sigma_\varepsilon\left(C_{\varepsilon,1} - C_{\varepsilon,2}\right) + \kappa^2 = 0$ [16]. Note that Eq. 13 is used for $z = z_H$ and $U = U_H$, together with the analytical solution for the turbulent kinetic energy in the log law: $k = u_*^2/\sqrt{C_\mu}$. However, the behavior of the k-ε-f_P EVM changes when the constant C_μ is modified, because C_μ is also present in f_P: $f_P(C_\mu)$, as explained in Sec. 2.2. Van der Laan et al. [13] showed that f_P reduces the wake recovery for lower values of C_μ, which correspond to a higher turbulence intensity in Eq. 14. This is unphysical, because higher turbulence levels should enhance mixing and increase the wake recovery. Therefore, the ambient turbulence intensity at hub height is set by changing the roughness height z_0 in Eq. 14 instead of C_μ. Subsequently, the friction velocity u_* is set using Eq. 13, such that the correct undisturbed hub height velocity is obtained. The changes in the stream-wise velocity profile are relatively small, especially at heights in the rotor area. For example, by physical site inspection one could argue to use a roughness height of 3 cm in the Western wake case of Wieringermeer (case one from Tab. II). The relative difference between the velocity profile using a roughness height of 3 cm and the roughness height calculated by the alternative way of controlling the turbulence level: $z_0 = 0.44$ cm is less than 0.1%, 2% and 5% at 120 m, 40 m and 20 m, respectively. In addition, there is often a high uncertainty in calculating the roughness from field measurements, which can be much larger than the difference in the turbulence adapted z_0. Furthermore, the measured velocity profile close to the ground is often influenced by local roughness variations that are not considered in the CFD simulations that use a uniform roughness height. It should be noted that the turbulent adapted z_0 can cause large differences in the velocity profile, for a case with a very low measured ambient turbulence intensity, located at a site with relatively large roughness. In this situation the turbulent adapted z_0 can become orders of magnitude smaller than the z_0 from site inspection. However, it is most likely that in such a measurement, the ambient turbulence

intensity is dictated by a stable ABL instead of the roughness height. These flows cannot be simulated with the current k-ε-f_P EVM, since it is calibrated for a neutral ABL in which the shear parameter $\tilde{\sigma}$ is a constant.

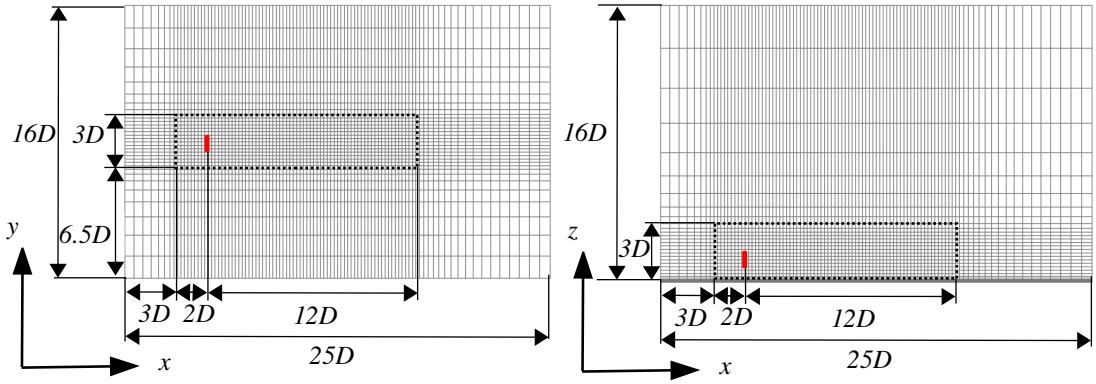

Figure 6. Computational domain RANS. Left: top view. Right: side view. Dashed black box marks the wake domain. Actuator disk is illustrated as a red filled box. One in every two nodes is shown.

Grid refinement study

The influence of the grid size on the flow solution for an AD in a uniform flow has been previously investigated in the work of Réthoré et al. [38]. This work was meant to verify the numerical procedure of the AD as implemented in EllipSys3D, by estimating the (mixed) order of the discretization error [39]. Therefore the grid study was performed such that all the individual components are at least second order accurate, i.e., a low Reynolds number was used such that a (low order) turbulence model is redundant. In addition, an analytical quadratic force distribution on the AD was used that made the behavior of the discretization error of the integrated force distribution second order accurate. From mixed order analysis Réthoré et al. showed that the AD method in EllipSys3D is still first order accurate [38]. In the grid study of the present research, the goal is to the estimate the discretization error of a more realistic setup, i.e., including a real wind turbine blade force distribution on the AD, applying a shear and using a high Reynolds number ($Re_D \sim 10^7$) that requires a turbulence model. It should be noted that the EllipSys3D AD method corrects for errors in the integrated force that arise from the discretization of the force distribution. Hence the same total force is used in each grid level, although distributed differently. One could argue that the use of a grid-independent total force is wrong, since a grid study of the same flow problem including the rotor geometry would have a total force that is dependent on grid size. On the other hand, one could claim that having a grid-independent total force is a feature of the AD method since it allows the use of coarser grids, which is the reason to use an AD in the first place.

The grid layout in the grid study is similar to the one presented in figure 6, but the stream-wise extent of the wake domain is chosen to be 10D in order to reduce the amount of cells. The number of cells in each grid level is given in Tab. III. A refinement ratio of two is used.

Table III. Computational grid size.

Grid level	Cells per rotor diameter in wake domain	Cells
1	32	9830400
2	16	1228800
3	8	153600
4	4	19200

The normalized momentum deficit at hub height $\langle U_{def}^2 \rangle$ taken from a volumetric horizontal straight section V is used to compare the solution on the different grid levels. $\langle U_{def}^2 \rangle$ is defined as:

$$\langle U_{def}^2 \rangle \equiv \frac{1}{U_{H,\infty}^2 V} \int_V (U_{H,\infty} - U(x,y,z))^2 \, dV, \tag{15}$$

where the normalization is carried out with the undisturbed hub height velocity $U_{H,\infty}^2$ and the integration volume V has dimensions $(\Delta x, \Delta y, \Delta z) = (0.5D, 3D, 0.5D)$. The comparison criterion is computed at three downstream distances from the AD: 2.5D, 5D and 7.5D. In order to make a fair comparison between the grid solutions, only cell centered values

Wind Energ. 2013; **00**:1–19 © 2013 John Wiley & Sons, Ltd.
DOI: 10.1002/we
Prepared using weauth.cls

are used within the volume V. The discretization error ϵ_n of each grid level n is estimated using a mixed order analysis [39]:

$$\epsilon_n = f_n - f_{h\to 0} = g_1 h_n + g_2 h_n^2 + g_3 h_n^3 + \mathcal{O}(h_n^4), \tag{16}$$

where f_n is the grid solution, $f_{h\to 0}$ is the extrapolated solution for an infinitely small grid size h_n and g_1, g_2, g_3 are the unknown constants to be evaluated. The finest grid size ($n = 1$) is set to unity ($h_1 = 1$) and the coarser grid sizes are defined as ($h_{n+1} = rh_n$), with r as the refinement ratio. Using the momentum deficit $\langle U_{def}^2 \rangle$ from Eq. 15 computed at the four grid levels of Tab. III, the discretization error can be estimated by disregarding fourth order errors $\mathcal{O}(h_n^4)$ and solving the corresponding closed system. The first order ($g_1 h_n$), second order ($g_2 h_n^2$) and third order ($g_3 h_n^3$) contributions to the total discretization error can now be investigated.

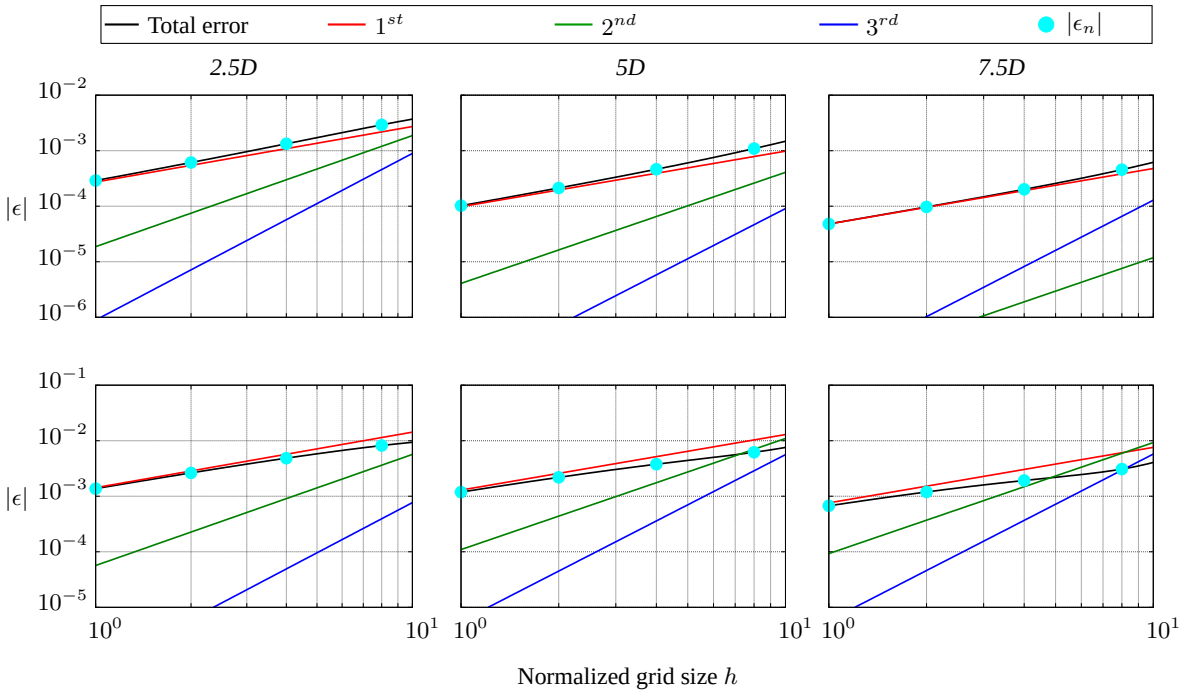

Figure 7. Order decomposition. Top row: k-ε EVM. Bottom row: k-ε-f_P EVM.

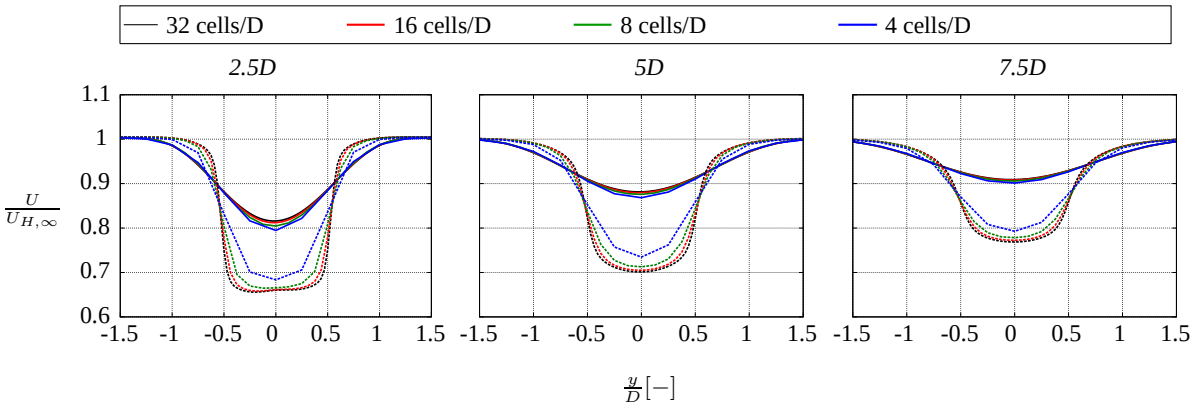

Figure 8. Wake deficit for different grid sizes with $D = 80$ m, $U_{H,\infty} = 10.7$ m/s, $I_{H,\infty} = 8\%$. Solid lines: k-ε EVM. Dashed lines: k-ε-f_P EVM with $C_R = 1.8$.

The grid study is performed for the k-ε EVM and the k-ε-f_P EVM using case one (Wieringermeer, see Tab. II). The discretization error and its first-, second- and third- order contributions are plotted in Fig. 7 at downstream distances of

2.5D, 5D and 7.5D. The k-ε EVM shows a very small discretization error. Even for the coarsest grid size the discretization error in terms of momentum deficit is smaller than 1% at all three downstream distances. The k-ε-f_P EVM, simulated with the original Rotta constant $C_R = 1.8$, is more sensitive to the grid size, although all errors are still below 1%. Note that higher values of C_R (as motivated in Sec. 4.2.2) will have discretization errors closer to the ones of the k-ε EVM, since the high gradients at the edge of the wake decrease with C_R. The decomposition of errors shows that the linear contribution is the dominant term in the discretization error for both turbulence models. The relative low mixed order is caused by the AD method, which is first order near the AD [38], and it is possibly degraded by the turbulence model further downstream from the AD.

The velocity deficit at the same three downstream distances is shown in Fig. 8. The deficit is extracted on a horizontal line at hub height, hence, an interpolation between the nearest cell centers is inevitable which makes it difficult to compare in absolute numbers. Nevertheless, the trends can be compared. The wake deficit in the k-ε EVM is not very sensitive to the used grid sizes, as observed before in mixed error analysis. However, the k-ε-f_P EVM shows larger deviations between grid solution, especially for the coarsest grid (four cells per rotor diameter in the wake domain). This is mainly caused by the fact that k-ε-f_P EVM predicts higher velocity gradients at the edge of wake compared to the standard k-ε EVM. The second coarsest grid (eight cells per rotor diameter in wake domain) show only small deviations from the two finer grids. Therefore, it is recommended to use at least eight cells per rotor diameter in the wake domain when using the k-ε-f_P EVM for wake simulations.

4.1.2. LES

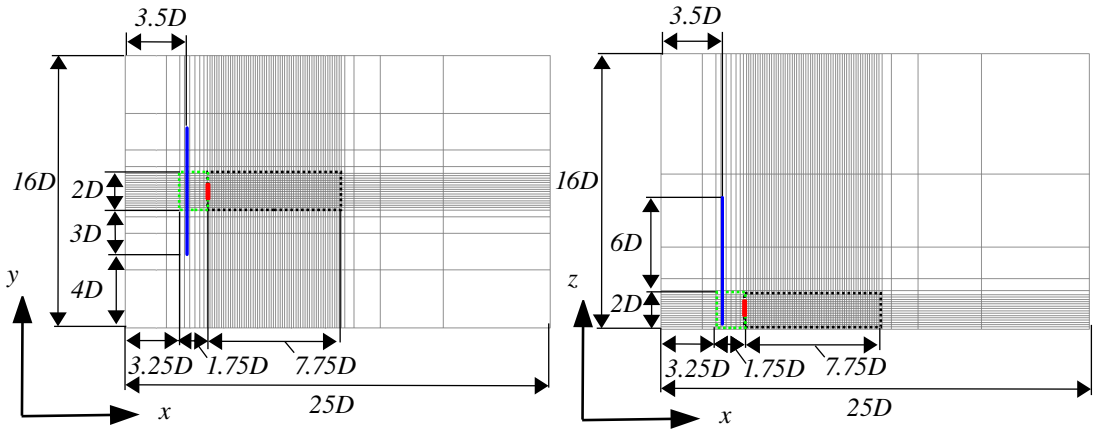

Figure 9. Computational domain LES. Left: top view. Right: side view. Dashed boxes: black is the wake domain and green marks the Mann turbulence domain. Actuator disk is illustrated as a red filled box. The inflow plane of Mann turbulence is shown as blue filled line. One in every eight nodes is shown.

The LES simulations are employed using the same AD as used in the RANS simulations and it is positioned in an equally sized domain. Fig. 9 shows the mesh where one in every eight nodes is plotted. The atmospheric turbulence is pre-calculated with the Mann model [40] and the results are scaled such that the correct total turbulence intensity, averaged at a cross section of 2D $\times$ 2D located in front of the wind turbine, is obtained. In this way, the same turbulent kinetic energy is felt by the wind turbine in the LES and in the RANS simulations. The domain of the Mann turbulence box is long enough to be able to describe one hour of turbulence plus the start up time of the LES simulation (which is disregarded when average results are calculated). The cross section of the Mann turbulence box is 8D $\times$ 8D and a uniform spacing with cell size D/8 is used in all directions. During the simulation the Mann turbulence is injected in a plane at 1.5D upstream of the AD. The injection plane is $8D$ wide, centered around the AD and it is extending $8D$ from the ground. This method is discussed in more detail in the work of Troldborg et al. [2, 28]. Two refined domains are defined in the flow domain: the wake domain 7.75D $\times$ 2D $\times$ 2D and the Mann turbulence domain 1.75D $\times$ 2D $\times$ 2D. In order to reduce the amount of cells, the wake domain in the LES simulations is smaller compared to the RANS simulations, however, it is still large enough to capture the wake up to 7.5D downstream. The wake domain is uniformly discretized with a cell size of D/60 in all directions, which is sufficient to resolve the wake [41]. The Mann turbulence domain is discretized with a cell size of D/30 in the stream-wise direction and it inherits the grid spacing from the wake domain for the other two directions. Note that there is smooth transition of cell size between the Mann turbulence domain and the Wake domain. The total domain consists of 17.7 million cells. The bottom boundary at $z = 0$ is modeled as a slip wall which, allows a first cell height equal to the uniform grid spacing in the wake domain, which saves a lot of cells compared to wall-resolved LES. The inlet conditions of the RANS simulations are also used in the LES simulations, however, a constant velocity of $u = u_*/\kappa \ln((z_H/10)/z_0)$

DOI: 10.1002/we
Prepared using weauth.cls

is set for $0 \leq z \leq z_H/10$ to comply with the slip wall. The rest of the boundaries are the same as used in the RANS simulations. Details of the numerical methods of the LES implementation are described in the work of Bechmann [42].

In order to maintain the log law solution of the neutral ABL in a LES simulation without a rough wall boundary, one could add small body forces in the entire domain [28]. However, it is not expected that the log-law solution decays significantly in reasonable vicinity of the AD, i.e. 7.5D downstream. In the current method the additional body forces are not included.

Even though the LES simulation is resolved in time, a constant forcing on the AD is applied. However, in terms of averaged wake deficit, a LES simulation using a constant force does not differ that much from one where time dependent forces are used [3].

The length of LES simulation is set such that one hour of converged data is gathered. The time integration in EllipSys3D is implicit, allowing the user to set very high CFL numbers. Nevertheless, the time step dt is set to a CFL number of one, i.e. $dt = dx/U_{H,\infty} = (D/60)/U_{H,\infty}$, such that the unsteady data is captured with a high resolution.

4.1.3. Calibration of C_R

The C_R parameter that is present in the k-ε-f_P EVM determines the wake deficits completely. In order to choose the right value of C_R, a calibration is carried out against the LES using the eight test cases that are described in Sec.3. The wake deficit at hub height, at the wake center (relative wind direction of 0°), at a downstream distance of 7.5D, is used to measure how well the k-ε-f_P EVM performs compared to LES. The results are shown in Fig. 10 in which the relative error ϵ_U of the wake deficit at the center at 7.5D is calculated as:

$$\epsilon_U = \frac{U_{RANS} - U_{LES}}{U_{LES}}. \tag{17}$$

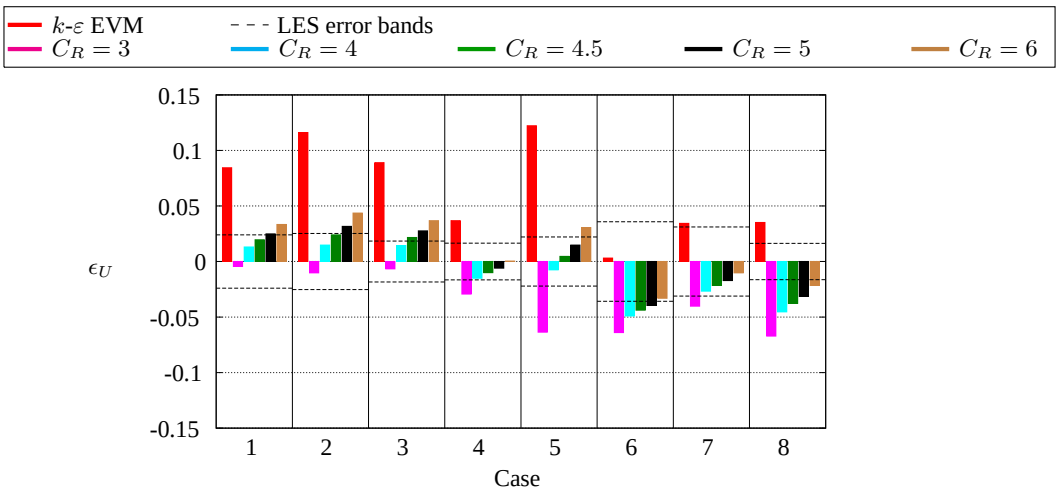

Figure 10. Calibration C_R

In Fig. 10 the error bars represent the uncertainty of the LES results, i.e., the standard deviations. In first seven cases, the wake center at 7.5D calculated by the k-ε-f_P EVM fits well LES when using $C_R = 4.5$. In case six, representing a case with a very high undisturbed turbulence intensity, the k-ε EVM performs better than the k-ε-f_P EVM at the far wake, although the result of the k-ε-f_P EVM with $C_R = 4.5$ does not exceed the standard deviation of LES significantly. Case eight shows that for a high thrust coefficient both the k-ε EVM and the k-ε-f_P EVM with $C_R = 4.5$ do not compare well with LES at 7.5D, however, both models have a comparable magnitude of ϵ_U.

4.2. Results and discussion

The results of the test cases based on measurements and the result for the test cases based on LES are shown in Fig. 11 and Fig. 12, respectively. The velocity wake deficit at hub height is plotted against the relative wind direction for a number of downstream locations. For the test cases based on measurements, the locations are chosen to match the measured ones. For case one, two and four, extra downstream locations are shown for comparison of the RANS results with the ones of LES. Note that downstream locations for test case four are normalized with $D^* = 40$ m instead of the real rotor diameter ($D = 41$ m) to comply with the normalization distance of the measurements. The wake deficit for test cases that are not based on measurements are plotted at 2.5D, 5D and 7.5D. For two of these cases (case five and six) the turbulence intensity

at hub height is given in Fig. 13. The results are shown for the k-ε EVM, the k-ε-f_P EVM with $C_R = 4.5$, LES and measurements. If available, the measurements are presented with error bars representing one standard deviation. The one hour LES simulations are averaged by using six bins of ten minutes. The standard deviation of the six bins are shown as error bars. For each case, the results of LES are normalized with the undisturbed hub height velocity taken from another LES simulation with the same setup but without using the AD. It has been found that in the case with a high undisturbed turbulence intensity (case six), the undisturbed hub height velocity at 7.5D deviates around 2% from the one that is imposed at the inlet. For all other cases the difference is much less, typically below 1%. A comparison of LES with measurements is given in Sec. 4.2.1 and Sec. 4.2.2, respectively.

4.2.1. LES compared to measurements

In the Western wake case from Wieringermeer (case one), shown in Fig. 11, the results of LES compare well with the available field measurements at 3.5D. Note that there is a clear offset of around 5 degrees in the measured wake center, which is probably caused by yaw error, as also discussed in the work of Schepers et al. [19]. The measurement of the Eastern wake case from Wieringermeer (case two) compares reasonably with the wake deficit predicted by LES, however, the magnitude of the maximum wake deficit is underpredicted by LES. Possible causes for the underpredicted wake deficit are effects of atmospheric stability on the measured wake deficit or the uncertainty in the prediction of the measured undisturbed turbulence intensity due to the lack of upstream measurements. The measured and the calculated wake deficit is asymmetric in the near wake (best visible in case two), which is caused by the interaction of wake rotation with a vertical shear, a phenomenon that is discussed in more detail in the work of Zahle and Sørensen [43].

In the Nibe case (case three) two different LES results are shown in Fig. 11: one with an average taken from of six bins of ten minutes and one with an averaging take from sixty bins of one minute. Since the measured wake deficit is processed with one minute averages it should be compared with the averaged LES results from the same bin length. The LES results for the ten minute bins are used to compare with RANS, as discussed in Sec. 4.2.2. A clear consequence of using one minute bins is the increase of the standard deviations compared to ten minute bins. This gives an idea of how large the standard deviations of the measurements can be. The measured wake deficit compares well with the results of LES at 2.5D and 7.5D. At 4D, the calculated wake deficit is slightly overpredicted compared to the measured one. However, assuming similar standard deviations for the measurements as observed in the LES results, obtained from one minute bins, the difference falls within the error bars. In addition, since the estimate of the undisturbed turbulence intensity in the measurements is very uncertain, as explained in Sec.3.2, it is difficult to compare the measurements with LES.

The lidar measurements of the Nordtank 500 wind turbine (case four) shows a similar trend in the wake deficits as the ones calculated with LES. However, at $1D^*$ the measurements do not show the clear double bell-shaped wake deficit as observed in LES. The AD method is least accurate in the near vicinity of the wind turbine and can explain the difference. For example, the forces of the nacelle are not present in the force distribution of the AD and it can lead to a lower wake deficit at the center of wake in AD simulations compared to the measurements. In addition, the measured wake deficit at $5D^*$ is more recovered compared to the one calculated by LES which is not fully understood. The uncertainty in the undisturbed turbulence intensity, terrain effects or large scale meandering are plausible causes for the difference in the wake recovery.

4.2.2. RANS compared to LES

Compared to LES, the wake deficit is underpredicted by the original k-ε EVM for all test cases at all downstream distances, as shown in Fig. 11 and Fig. 12, except for case six and seven at the far wake. These cases correspond to a high undisturbed turbulence intensity and low thrust coefficient. The k-ε EVM performs the worst for a high thrust coefficient (case three and case eight) and for a low turbulence intensity (case two and case five).

All cases show that the near wake deficits calculated by k-ε-f_P EVM, are much closer to the ones of LES, compared to the ones of the original k-ε EVM. The largest improvement in the near wake deficits is obtained for the cases with a low turbulence intensity and a high thrust coefficient.

In the work of Réthoré [3], it has been found that the k-ε EVM overestimates the turbulence intensity of the wake. A similar result for the case with a low undisturbed turbulence intensity (case five) at 2.5D is shown in Fig. 13. In this case, the turbulence intensity predicted by k-ε-f_P EVM is more comparable with LES, however, at 7.5D both EVMs overpredict the turbulence intensity. In the high turbulence case (case six), the same conclusion can be made but the difference between RANS and LES is smaller than seen in case five because of the high level of background turbulence. Note the calculated turbulence intensity in LES simulations deteriorates outside the wake domain (relative wind directions larger than $\approx \pm 10$ $^\circ$at 7.5D) because the of increasing cell size.

Wind Energ. 2013; **00**:1–19 © 2013 John Wiley & Sons, Ltd.
DOI: 10.1002/we
Prepared using weauth.cls

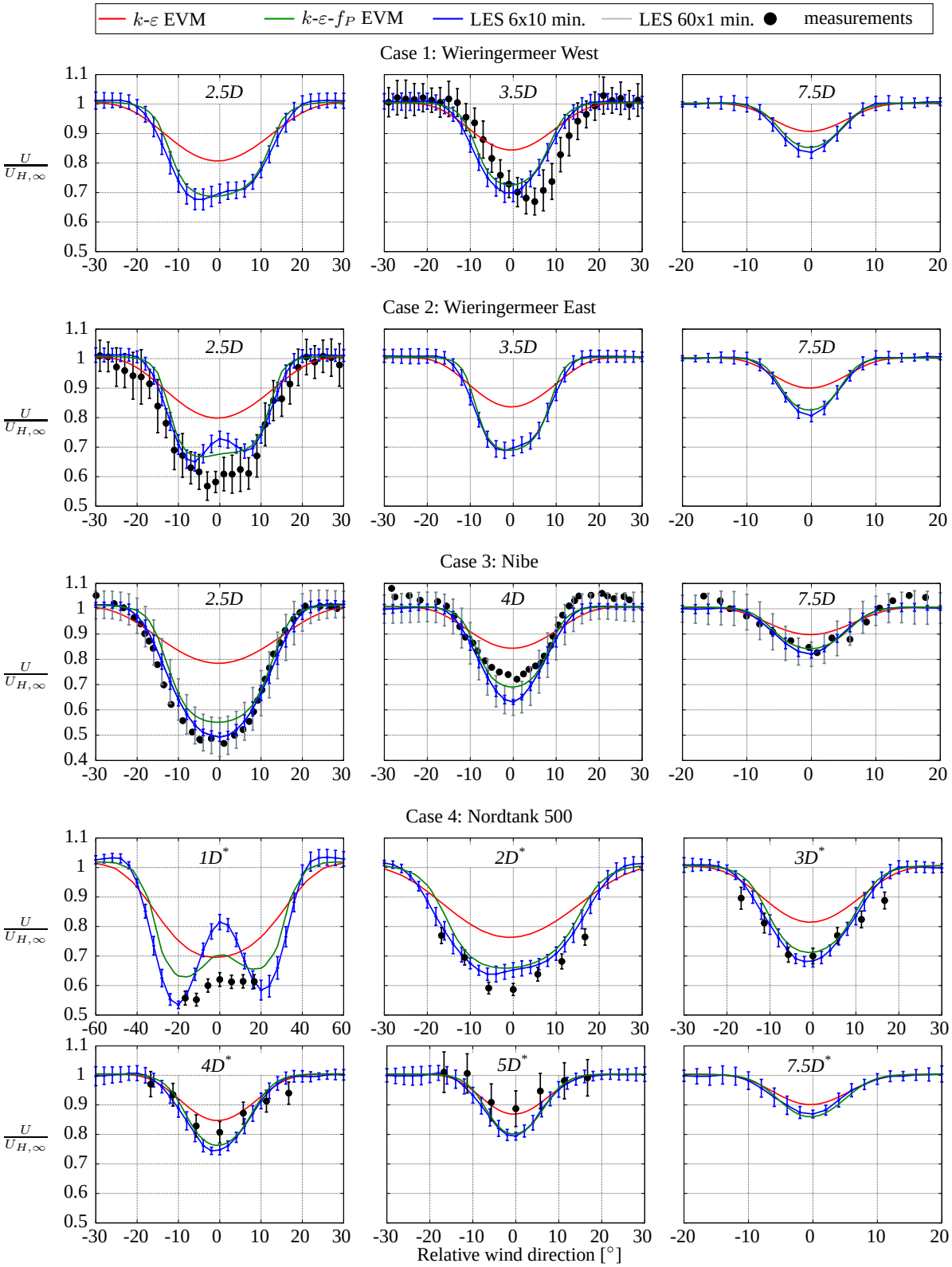

Figure 11. Test cases based on field measurements. The measurements and the LES results include error bars of one standard deviation. $C_R = 4.5$ in k-ε-f_P EVM.

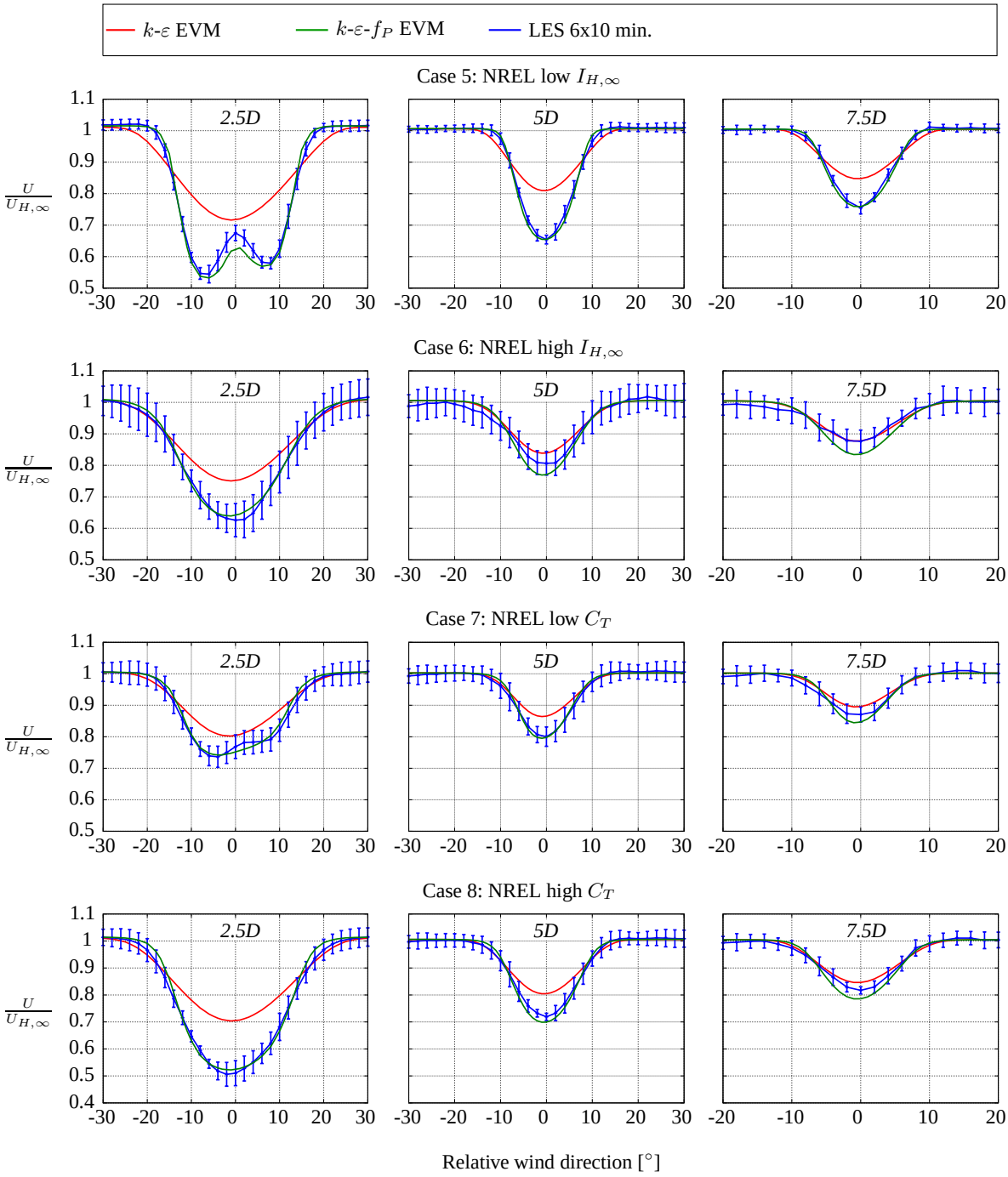

Figure 12. Additional test cases based on LES. The LES results include error bars of one standard deviation. $C_R = 4.5$ in k-ε-f_P EVM.

Wind Energ. 2013; **00**:1–19 © 2013 John Wiley & Sons, Ltd.
DOI: 10.1002/we
Prepared using weauth.cls

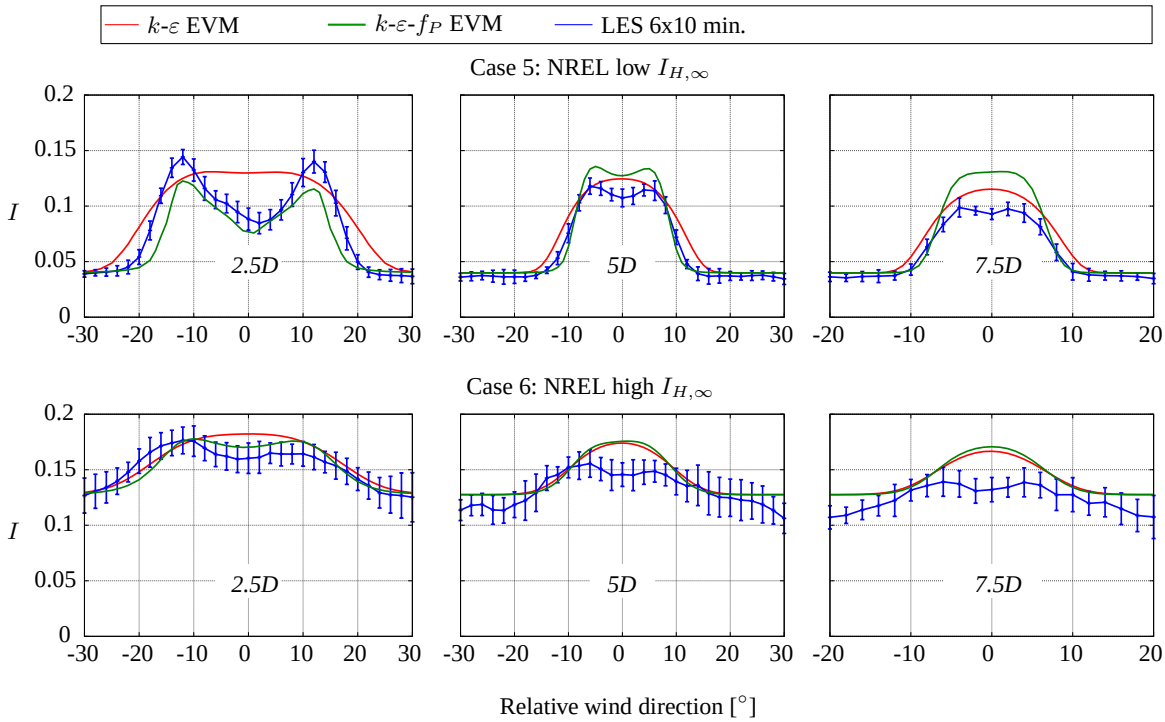

Figure 13. Turbulent intensity $I = \sqrt{2/3k}/U_{H,\infty}$ for test case five and six. The LES results include error bars of one standard deviation. $C_R = 4.5$ in k-ε-f_P EVM.

4.2.3. Computational cost

The computational effort of the simulations of all test cases are given in Tab. IV. All simulations are carried out on the same cluster, however, a different number of nodes have been used: fifteen for LES and three for RANS simulations, except for case five which has been calculated with five nodes for the RANS simulations. Each node has two Intel Xeon X5650 processors with six cores each that have a clock frequency of 2.66 GHz. In most cases, the LES simulations are approximately 10^3 computationally more expensive compared to the RANS simulations The RANS simulations of case five are computationally more expensive because the low turbulence intensity is represented by a very low roughness. Hence, more cells are necessary in the grid and the convergence of the numerical scheme is slowed down. The large mesh and the simulation time that is needed to gather enough unsteady data, makes the LES very expensive, especially when a small wind turbine is used which limits the time step (time step is proportional to the rotor diameter). The difference in computational effort between the two RANS turbulence models is negligible. Note that the comparison is only a rough estimate since a different number of nodes are employed for the LES and the RANS simulations. In addition, the cluster is also used by others which can influence the effective computational effort.

Table IV. Computational effort in CPU hours of the single wake simulations.

	LES	RANS k-ε	RANS k-ε-f_P ($C_R = 4.5$)
case 1	5360	4.2	4.6
case 2	5341	3.3	3.5
case 3	11036	3.0	3.9
case 4	10559	3.5	4.1
case 5	2749	25	28
case 6	2743	5.7	5.6
case 7	2747	3.9	5.2
case 8	2784	4.0	5.4

5. CONCLUSIONS

A modified k-ε EVM with a flow-dependent C_μ (called C_μ^*) is proposed: the k-ε-f_P EVM. C_μ^* decreases the eddy viscosity in regions with high velocity gradients, e.g., in a wind turbine wake. The impact of C_μ^* on the flow solution is controlled by a parameter C_R which is calibrated with LES for eight different single wake cases. From the calibration it is recommended to use $C_R = 4.5$. Four of the eight test cases are based on measurements and their results compare reasonably well with LES. However, the comparison with measurements is limited because the uncertainty in the undisturbed turbulence intensity is large and the effects of stability are not filtered out for three of four measured wake cases.

A grid refinement study has shows that the k-ε-f_P EVM is more sensitive to grid size compared the original k-ε EVM. Nevertheless, both turbulence models show discretization errors below 1% for a grid spacing of D/8 in the wake region.

Where the original k-ε EVM underpredicts the velocity wake deficit compared to LES and measurements, the k-ε-f_P EVM shows more comparable results with respect to LES, for seven of the eight wake cases. These improvements are mainly observed for the test cases in which k-ε EVM has the worst performance, i.e., a low turbulence intensity and a high thrust coefficient. On the contrary, the test case with a high (total) turbulence intensity (12.8%) shows that the wake recovery of LES is closer to the original k-ε EVM. However, in the near wake the k-ε-f_P EVM is superior to the k-ε EVM for all eight cases. The fact that the k-ε-f_P EVM is approximately 10^3 computationally less expensive than LES and it has the same numerical stability as the original k-ε EVM, makes the k-ε-f_P EVM an attractive turbulence model which has the potential to simulate wake effects on the power production of wind farms.

ACKNOWLEDGEMENTS

This work is supported by the Center for Computational Wind Turbine Aerodynamics and Atmospheric Turbulence funded by the Danish Council for Strategic Research, grant number 09-067216. Computational resources were provided by DCSC and the DTU central computing facility.

REFERENCES

1. Barthelmie RJ, Frandsen ST, Nielsen NM, Pryor SC, Réthoré PE, Jørgensen HE. Modelling and measurements of power losses and turbulence intensity in wind turbine wakes at Middelgrunden offshore wind farm. *Wind Energy* 2007; **10**:217–228.
2. Troldborg N, Larsen GC, Madsen HA, Hansen KS, Sørensen JN, Mikkelsen R. Numerical simulations of wake interaction between two wind turbines at various inflow conditions. *Wind Energy* 2011; **14**:859–876.
3. Réthoré PE. Wind Turbine Wake in Atmospheric Turbulence. PhD Thesis, Risø 2009.
4. Cabezón D, Migoya E, Crespo A. Comparison of turbulence models for the computational fluid dynamics simulation of wind turbine wakes in the atmospheric boundary layer. *Wind Energy* 2011; **14**:909–921.
5. El Kasmi A, Masson C. An extended k-ε model for turbulent flow through horizontal-axis wind turbines. *Journal of Wind Engineering and Industrial Aerodynamics* 2008; **96**:103–122.
6. Prospathopoulos JM, Politis ES, Rados KG, Chaviaropoulos PK. Evaluation of the effects of turbulence model enhancements on wind turbine wake predictions. *Wind Energy* 2011; **14**:285–300.
7. Boussinesq MJ. *Théorie de l'écoulement tourbillonnant et tumultueux des liquides*. Gauthier-Villars et fils, 1897.
8. Pope SB. *Turbulent Flows*. Cambridge University Press, 2005.
9. Chen YS, Kim SW. Computation of turbulent flow using an extended turbulence closure model. *NASA Contractor Report CR-179204*, NASA 1987.
10. Shih TH, Liou WW, Shabbir A, Yang Z, Zhu J. A new k-ε eddy viscosity model for high Reynolds number turbulent flows-model development and validation. *Technical Report*, NASA 1994.
11. Apsley DD, Leschziner MA. A new low-Reynolds-number nonlinear two-equation turbulence model for complex flows. *International Journal of Heat and Fuid Flow* 1998; **19**:209–222.
12. Taulbee DB. An improved algebraic Reynolds stress model and corresponding nonlinear stress model. *Physics of Fluids* 1992; **A4 11**:2555–2561.
13. van der Laan MP, Sørensen NN, Réthoré PE, Mann J, Kelly MC, Schepers JG. Nonlinear Eddy Viscosity Models applied to Wind Turbine Wakes. *Proceedings of International Conference on Aerodynamics of Offshore Wind Energy Systems and Wakes 2013*; 514–525.
14. Gómez-Elvira R, Crespo A, R, Migoya E, Manuel F, J H. Anisotropy of turbulence in wind turbine wakes. *Journal of Wind Engineering and Industrial Aerodynamics* 2005; **93**:797–814.
15. Launder BE. An introduction to single-point closure methodology. *Simulation and Modeling of Turbulent Flows*, Gatski TB, Hussaini MY, Lumley JL (eds.), New York: Oxford University Press, 1996; 243–310.

16. Richards PJ, Hoxey RP. Appropriate boundary conditions for computational wind engineering models using the k-ε turbulence model. *Journal of Wind Engineering and Industrial Aerodynamics* 1993; **46,47**:145–153.
17. Rotta JC. Statistische Theorie nighthomogener Turbulenz. *Z. Physics* 1951; **129**:547–572.
18. Launder BE, Reece GJ, Rodi W. Progress in the development of a Reynolds-stress turbulence closure. *Journal of Fluid Mechanics* 1975; **68**:537–566.
19. Schepers JG. Analysis of wake measurements from the ECNWind Turbine Test Site Wieringermeer, EWTW. *Wind Energy* 2012; **15**:575–591.
20. Taylor GJ. *Wake measurements on the Nibe turbines in Denmark*. ETSU WN 5020, National Power - Technology and Environment Centre, 1990.
21. Machefaux E, Larsen GC, Rettenmeier A. Single Wake Meandering, Advection and Expansion - an analysis using an adapted Pulse Lidar and CFD LES-ACL simulations. *Scientific proceedings of EWEC 2013*; 50–55.
22. Machefaux E, van der Laan MP, Hansen KS, Réthoré PE, Larsen GC, Schlipf D, Rettenmeier A. Wakebench: nacelle-based wake lidar measurements for model performance assessment. *Wind Energy* ; Planned to submit in 2014.
23. Jonkman J, Butterfield S, Musial W, Scott G. Definition of a 5-MW Reference Wind Turbine for Offshore System Development. *Technical Report*, National Renewable Energy Laboratory 2009.
24. Panofsky HA, Dutton JA. *Atmospheric Turbulence*. Wiley-interscience, 1984.
25. International standard IEC 614001, 1999.
26. Schepers JG. Personal communication 2012; .
27. Lindenburg C, Snel H. PHATAS-II: program for horizontal axis wind turbine analysis and simulation version II. *Technical Report*, ECN-C–93-038 1993.
28. Troldborg N, Sørensen JN, Mikkelsen R, Sørensen NN. A simple atmospheric boundary layer model applied to large eddy simulation of wind turbine wakes. *Wind Energy* 2013; Published online.
29. Troldborg N, Zahle F, Sørensen NN, Réthoré PE. Comparison of wind turbine wake properties in non-uniform inflow predicted by different rotor models. *Torque conference 2012, Oldenburg, Germany*, 2012.
30. Troldborg N, Zahle F, Sørensen NN, Réthoré PE. Comparison of wind turbine wake properties in non-sheared inflow predicted by different CFD rotor models. *Wind Energy* ; Submitted, May 2013.
31. Sørensen NN. General purpose flow solver applied to flow over hills. PhD Thesis, Technical University of Denmark 1994.
32. Michelsen JA. Basis3d - a platform for development of multiblock PDE solvers. Technical report AFM 92-05,. *Technical Report*, Technical University of Denmark, Lyngby 1992.
33. Patankar SV, Spalding DB. A calculation procedure for heat, mass and momentum transfer in three-dimensional parabolic flows. *International Journal of Heat and Mass Transfer* 1972; **15**:1787–1806.
34. Leonard BP. A stable and accurate convective modelling procedure based on quadratic upstream interpolation. *Computer Methods in Applied Mechanics and Engineering* 1979; **19**:59–98.
35. Réthoré PE, Sørensen NN. A discrete force allocation algorithm for modelling wind turbines in computational fluid dynamics. *Wind Energy* 2012; **15**:915–926.
36. Rhie CM, Chow WL. Numerical study of the turbulent fow past an airfoil with trailing edge separation. *AIAA Journal* 1983; **21**:1525–1532.
37. Mikkelsen R. Actuator Disc Methods Applied to Wind Turbines. PhD Thesis, Technical University of Denmark, Mek dept 2003.
38. Réthoré PE, van der Laan MP, Troldborg N, Zahle F, Sørensen NN. Verification and validation of an actuator disc model. *Wind Energy* 2013; Published online.
39. Roy CJ. Grid Convergence Error Analysis for Mixed-Order Numerical Schemes. *American Institute of Aeronautics and Astronautics Journal* 2003; **41**(4).
40. Mann J. The spatial structure of neutral atmospheric surface-layer turbulence. *Journal of Fluid Mechanics* 1994; **273**:141–168.
41. Troldborg N, Sørensen JN, Mikkelsen R. Numerical simulations of wake characteristics of a wind turbine in uniform inflow. *Wind Energy* 2010; **13**:86–99.
42. Bechmann A. Large-Eddy Simulation of Atmospheric Flow over Complex Terrain. PhD Thesis, DTU-MEK, Denmark 2007.
43. Zahle F, Sørensen NN. Overset grid flow simulation on a modern wind turbine. *AIAA-2008-6727*, 2008.